16th World Conference on Earthquake, 16WCEE 2017

Santiago Chile, January 9th to 13th 2017

Paper N° 4602

Registration Code: S-R1464029330

SLIP MODEL OF THE 2015 M_W 8.3 ILLAPEL (CHILE) EARTHQUAKE FROM INVERSION OF SENTINEL 1A AND GPS DATA.

P. Aguirre[(1)], C. Fortuño[(2)], J.C. de la Llera[(3)], C. Wicks[(4)], G. González[(5)], J.Cembrano[(6)].

(1) Adjunct Assistant Professor, School of Engineering, Pontificia Universidad Católica de Chile, National Research Center for Integrated Natural Disaster Management CONICYT/FONDAP/15110017, paula.aguirre@cigiden.cl
(2) Researcher, School of Engineering, Pontificia Universidad Católica de Chile, National Research Center for Integrated Natural Disaster Management CONICYT/FONDAP/15110017, catalina.fortuño@cigiden.cl
(3) Professor, School of Engineering, Pontificia Universidad Católica de Chile, PI National Research Center for Integrated Natural Disaster Management CONICYT/FONDAP/15110017, jcllera@ing.puc.cl
(4) Research Geophysicist, U.S. Geological Survey, Menlo Park, CA, USA, cwicks@usgs.com
(5) Professor, Universidad Católica del Norte, PI National Research Center for Integrated Natural Disaster Management CONICYT/FONDAP/15110017, ggonzale@ucn.cl
(6) Professor, School of Engineering, Pontificia Universidad Católica de Chile, National Research Center for Integrated Natural Disaster Management CONICYT/FONDAP/15110017, jcembrano@ing.puc.cl

Abstract

The M_w 8.3 earthquake that occurred on September 16th 2015 west of Illapel, Chile, ruptured a ~200 km section of the plate boundary between 29°S and 33°S. SAR data acquired by the Sentinel 1A satellite was used to obtain the interferogram of the earthquake, and from it, the component of the displacement field of the surface in the line of sight of the satellite. Based on this interferogram, the corresponding coseismic slip distribution for the earthquake was determined based on different plausible finite fault geometries. The model that best fits the data gathered is one whose rupture surface is consistent with the Slab 1.0 model, with a constant strike angle of 4° and variable dip angle ranging from 2.7° near the trench to 24.3° down dip. Using this geometry the maximum slip obtained is 7.52 m and the corresponding seismic moment is $3.78 \cdot 10^{21}$ equivalent to a moment magnitude M_w 8.3. The interferogram processed is also used to analyze specific site effects, such as deformations found in areas of affected mining tailing dams. A comparison between this earthquake rupture model and the inversion models of two previous earthquakes, the M_w 8.2 Pisagua (Chile, 2014) and the M_w 8.8 Maule (Chile, 2010) is done to study different earthquake characteristics, and provide a suite of methodologically consistent and spatially detailed characterizations of the fault rupture mechanisms and the permanent superficial effects of megathrust events along the Chilean coastline. These results are a key input for the generation of synthetic seismic records that combine deterministic and stochastic methods for representation of low- and high-frequency components of ground motions, respectively, and will hence enable us to characterize the seismic demand for both flexible and rigid structures in earthquake-affected areas, and thereby investigate the direct damage and losses that may be expected during future events.

Keywords: InSAR; Illapel; slip model.

1. Introduction: the 2015 Mw 8.3 Illapel Earthquake.

A segment of the subduction zone located in the central coast of Chile was activated on September 16th 2015 at 22:54:33 UTC generating a magnitude M_W 8.3 (M_0=2.85×10^{21} N·m) megathrust earthquake with hypocenter located offshore the coast of the Coquimbo region (31.57º S, 71.654º W), 48 km west of the town of Illapel at a depth of 25 km [1]. The event generated a Pacific Ocean tsunami with maximum wave heights of 4.5 m in Coquimbo and 1.9 m in Valparaíso, which triggered the evacuation of more than 1 million people along the Chilean coastline. In combination, the earthquake and tsunami resulted in a death toll of 15 people, 2281 destroyed houses, 2404 houses with major structural damage [2], and partial damage in eight bridges and the road network.

Preliminary calculations of the Global Centroid-Moment Tensor solution (CMT; [3,4]) and slip distribution based on seismic data show that the earthquake ruptured a section of approximately 280 km parallel to the boundary between the Nazca and South American plates with a thrust focal mechanism with centroid at (31.22ºS, 72.27ºW). The fault plane geometry was originally defined by a strike angle of 5º, dip of 22º, and rake of 106º. The main event was followed by a sequence of ca. 1900 aftershocks within the following two months, 26 of them with magnitudes $M_W \geq 6.0$ ([4], see Fig. 5).

Previous work on geodetically derived coupling [6] inferred that the segment that slipped during this event was characterized by a coupling coefficient between 31% and 69%. Seismic activity records for the 30º-33.5º S segment, identified as the Metropolitan Segment [6], reveal a history of major subduction earthquakes, including events in 1730 (M_S 8.5 to 9.0, [7]), 1822 (M_S 8-8.5, [7]), 1880 (M_S 7.5, [8]), 1873 (M_S 7.5, [9]), 1906 (M_l 8.6, [10]), 1943 (M_w 7.9, [11]), 1971 (M_S 7.5, [12]), and 1985 (M_w 8.0, [9]). Approximate rupture lengths and location of these earthquakes are depicted in Figure 1. The nature and number of earthquakes identified above show that the segment activated by the 2015 earthquake had ruptured completely during the 1730 event, and partially during lesser magnitude episodes. In particular, the 1880 and 1943 events seem to have ruptured part of the same region as the 2015 event.

In this work, we use Synthetic Aperture Radar (SAR) data from satellite Sentinel 1A to generate a high-resolution map of the coseismic slip of the M_W 8.3 Illapel earthquake, and in combination (or not) with continuous GPS data from the Centro Sismológico Nacional (CSN; [5]), carry out an inversion model to determine the slip distribution of the plate interface. Based on this slip distribution, we are able to estimate the stress changes in the ruptured area, and correlate with the observed sequences of aftershocks and previous knowledge on the region's tectonic and geological setting in order to understand the remaining seismic potential of the plate segment. We start with a more detailed discussion of the tectonic and geological context for the Illapel region in Section 2; in Section 3 we describe the data and methods applied to obtain slip models for the 2015 earthquake. Our results are presented in Section 4, and in Section 5 we discuss the Illapel earthquake faulting mechanism in the context of recent major Earthquakes in Chile (Maule 2010 and Pisagua 2014). Finally, we summarize our conclusions in Section 6.

2. Tectonic and Geological Context.

In the area hit by the 2015 M_W 8.3 Illapel earthquake, the Nazca and South American plates converge at a rate of about 68 mm/yr [6]. Convergence is nearly orthogonal to the trench, with a low obliquity angle of ca. 20º with respect to trench normal. The area is characterized by a nearly horizontal slab geometry that results in the absence of active volcanoes in the overriding plate [13]. The down-going Nazca Plate between 30º and 33º S contains two first-order morphological features of the ocean floor: the Challenger fracture zone (CFZ) to the north and the Juan Fernandez ridge (JFR) to the south (e.g. [14, 15]). These fractures appear to mark the northern and southern bounds of the rupture zones in the 1880 (M_s 7.5) and 1943 (M_w 7.9) earthquakes (Fig. 1). According to Tichelaar and Ruff [14], there is a change in slab dip north and south of the CFZ, from ca. 16º to 23º, which can account for different seismicity patterns along the subduction zone. Furthermore, along the eastward projection of the CFZ, the continental margin exhibits a regional E-N-E discontinuity associated with a

jump on the dominant north-south spatial distribution of major geological units (Fig. 1). Regarding the long-term deformation pattern of the Andean margin, the northern edge of the Illapel´ s earthquake rupture zone also coincides with the southern limit of the Vallenar orocline as suggested by paleomagnetic data (e.g. [16]).

The coastal region of the area of the Illapel earthquake shows some singular features in coastal morphology and in the geological structure of the upper plate. The existence of the Talinay Peninsula and the major bays of Tongoy and Coquimbo mark the boundary of major historical ruptures of the megathrust, as the ones in 1730 and 1822, highlighting the northernmost boundary of the Metropolitan Segment and the southernmost boundary of the Atacama Segment, as defined by Métois et al. [6]. From a geological point of view, the boundary between the Mesozoic igneous rock of the Coastal Cordillera and the Neogene deposits to the east is marked by the NS-striking, east-dipping, Puerto Aldea fault (PAF), running for more than 50 km from the Tongoy Bay area to the south (Fig. 1). The PAF has been described as a neotectonic fault with a potential to produce M_W 7 earthquakes, according to long-term geological observations (e.g. [17]). Furthermore, this neotectonic fault can be regarded as an upper plate discontinuity, which may be related to the subduction zone seismic cycle. In this sense, the PAF represents one example of a series of north-striking faults present along large portions of the forearc in north Chile. These faults may accommodate geologically instantaneous extension arising from differential margin-orthogonal displacement during and after subduction mega-earthquakes (e.g. [18, 19, 20]).

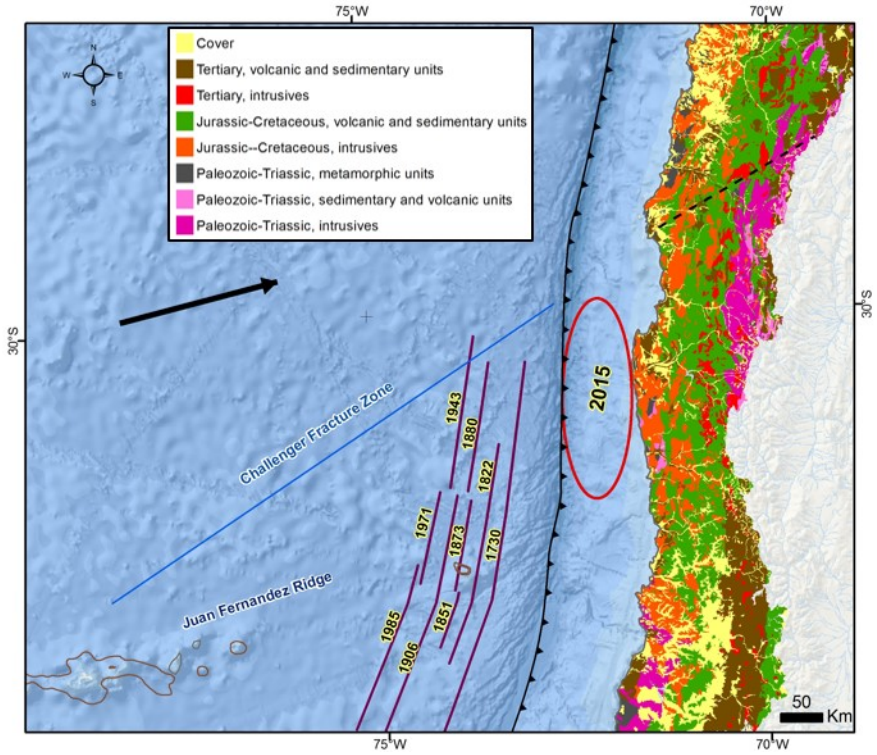

Fig. 1 – Seismotectonic settting for the Illapel earthquake area. The colormap represents the distribution of major geological units; also shown are the locations of the oceanic trench (black triangled line), the Challenger Fracture Zone (blue solid line) with its eastward projection (black dashed line), and the Juan Fernández Ridge. Approximate rupture lengths and locations of historical earthquakes are represented as solid purple segments, and the rupture area of the 2015 Illapel earthquake is marked in red. The black solid arrow indicates the convergence direction of the Nazca and South American plates.

3. Data and Methods.

The faulting mechanisms and source parameters of earthquakes can be constrained from measurement of

the short-term crustal deformations caused by the main shock, and the application of finite-fault inversion methods to infer the distribution of slip in the plate interface. Different geodetic methods are currently applied to obtain detailed characterizations of the 3-D coseismic displacement field, including synthetic aperture radar interferometry (InSAR), which yields millimeter-precision measurements of displacements over extended spatial scales, and analysis of GPS data, that provide continuous temporal sampling of surface deformations.

In InSAR, two temporally-separated satellite SAR images are obtained at the same location during the ascending (South – North) or descending (North – South) orbit, which provide different observation angles. The measured phase differences are used to create a map of surface deformations in the direction of the line-of-sight (LOS) of the satellite, known as interferogram [21 , 23]. To model the coseismic field for the Illapel earthquake, we use three slices of C-band Sentinel 1A SAR data acquired between August and September of 2015 (see details in Table 1) to construct ascending and descending interferograms and, hence, determine LOS displacements. For each path we constructed three geocoded interferograms (one for each slice), which were then mosaicked together seamlessly. Because the incidence angle of the radar varies considerably across the swath, we also calculated maps of radar incidence angle for use in modeling of the slip distribution. Data were processed within the GAMMA software [24] following standard algorithms.

Table 1 – Technical Specifications of Sentinel 1A Data. Orbit parameters and dates of pre- and post-earthquake SAR images used for computation of ascending and descending interferograms.

Relative Orbit	**Orbit Direction**	**Slices**	**Pre-earthquake Date**	**Post-earthquake Date**	**Perpendicular baseline $B_\perp$ (m)**
156	Ascending	12,13,14	20150824	20150917	115
18	Descending	8,9,10	20150826	20150919	75

Horizontal and vertical displacement measurements from nine continuous GPS stations operated by CSN (Chile) at latitudes between 29.55º and 32.55ºS where also incorporated into the inversion model. These data were processed with the GAMIT/GLOBK software, and corrected for orbital, ionospheric, tropospheric, and instrumental effects.

The coseismic slip distribution is determined by performing a typical linear seismic inversion, where the forward problem determines the surface displacements (here determined from InSAR and GPS measurements) produced by a distribution of rectangular source dislocations within an elastic medium (i.e., a discretized fault slip distribution). The linear closed-form solution to this problem is contained in the well-known suite of analytical expressions by Okada [22], which lead to an over-determined system of linear equations that is solved using similar mathematical and computing techniques as those described in previous work (e.g. [26, 27, 28]). We repeat this procedure using the InSAR/GPS datasets both separately and combined, so as to probe the dependency between the estimated slip distribution, and the different types of surface displacement measurements considered.

Once a fault geometry and slip distribution model is obtained, we investigate the stress generated by the fault slip into the surrounding crust by computing the associated changes in normal and shear stress, following again Okada´s solution for an elastic half-space with uniform isotropic properties [29]. While the occurrence of an earthquake is expected to produce an overall reduction of stress accumulated over long periods of plate convergence, it may also result in tectonic loading of contiguous fault segments, and hence induce subsequent seismic events (e.g. [30,31]). Triggering of slip in nearby faults is related to changes in the Coulomb failure stress (CFS), defined as $\Delta CFS=\Delta\tau+\mu\Delta\sigma$ where $\Delta\tau$ is the change in shear stress (positive in the slip direction), $\Delta\sigma$ is the change in normal stress (positive when the fault is unclamped), and μ is the apparent friction coefficient after accounting for the pore fluid pressure effect [30]. In this criterion, failure in a secondary or receiver fault is promoted when slip on the source fault increases the Coulomb stress, so areas where $\Delta CFS>0$ are recognized as more likely locations of subsequent seismic activity. For analysis of the Illapel earthquake sequence, we model the CFS change over the main shock faulting surface after the initial *Mw* 8.4 event, using

the *Coulomb 3* software [31,32], and assuming an apparent friction coefficient μ=0.4, as suggested in the literature for subduction zones [31].

4. Results: Interferogram, Slip Model and Coulomb Failure Stress for the Illapel Earthquake.

The resulting ascending and descending interferograms obtained for the 2015 Illapel earthquake are presented in Fig. 2. In these diagrams, the pattern of interference fringes represent a series of contours of equal surface displacement with respect to a reference, where each successive cycle of colors (red to blue) indicate an increase in the distance between the ground and the satellite of 100 mm. Assuming zero displacement in the far field, it is possible to count 14 fringes that add up to a maximum line-of-sight deformation of ~1.4 m at latitude ~31º S. Please note though that the descending interferogram, based on SAR images obtained on September 17th, includes the effect of the M_w 7.0 aftershock of September 16th 23:18:35 UTC. Detailed inspection of local interferogram features results in the detection of anomalies corresponding to specific site effects, such as deformations in tailing dams. As an example, shown in the right panel of Fig. 3 is a closed-up view of the descending interferogram for an area of roughly 110 km^2 around the Los Pelambres copper mine, showing coseismic deformations of the order of 0.5-0.6 m (two fringes of 27.7 mm deformation each). These site effects and their consequences on the stability of potentially hazardous structures will be investigated in further detail in upcoming work.

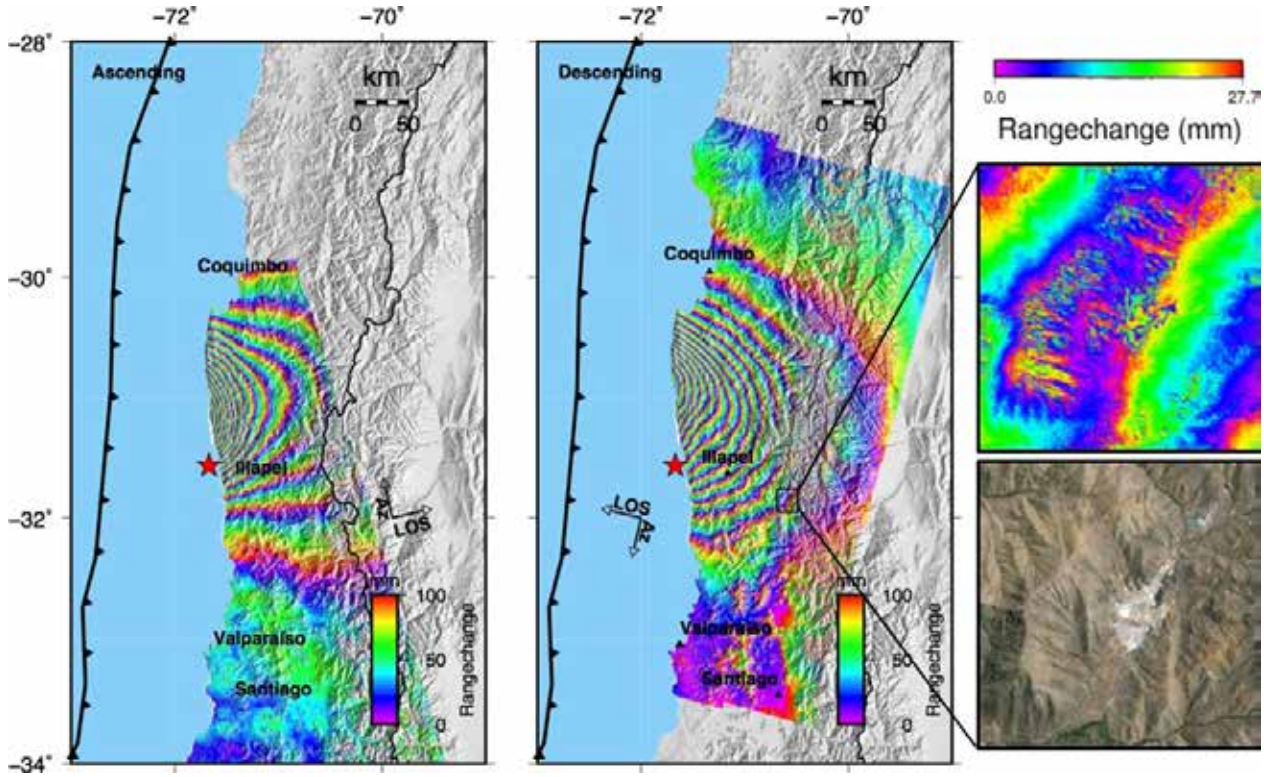

Fig. 2 – Ascending and Descending Sentinel 1A interferograms for the Illapel earthquake. In the left and center panels, colormaps represent the field of coseismic displacements in the direction of the satellite's line-of-sight (indicated by the black arrows), with each fringe denoting an increase in deformation of 100 mm. In both cases we register a total of 14 fringes, which account for a total deformation of 1.4 meters. The black triangle lines indicate the location of the oceanic trench, and the red stars mark the earthquake's epicenter. Panels on the right show a zoomed-in view of the descending interferogram and public satellite imagery (Google Earth) around Los Pelambres tailing dam. In this case, each color fringe represents a deformation of 27.7 mm, as indicated by the colorbar at the top.

Using the interferograms described above and the GPS displacement measurements (both separately and combined) different plausible finite fault geometries were tested considering the rapid USGS solution as a starting point [33]. The solution that provides and optimal fit to the different datasets is one whose rupture surface is consistent with the Slab 1.0 model [34], which provides a constant strike of 4º and variable dip angle ranging from 2.7º to 24.3º. This plane is 420 km long and 160 km wide and is subdivided into 672 sub faults of 10×10 km each. The epicenter was located at 31.57ºS and 71.654ºW, which is consistent with the published USGS solution [33]. In our calculations, we adopted a shear modulus $\mu = 33$ GPa, following a previous study by Béjar-Pizarro et al. [35]. The results obtained using InSAR, GPS, and INSAR+GPS data are shown in Fig. 3, where color maps correspond to total slip magnitudes in each sub fault, and arrows in the smaller right-side panels indicate the slip vector directions.

In Fig. 3a, we show the slip distribution estimated using only InSAR co-seismic displacements The model shows a single slip patch nearly 200 km long, with centroid located north-west of the city of Illapel that closely matches the rupture zone of the 1943 earthquake. The maximum slip obtained is 7.2 m, and the corresponding seismic moment is 3.60×10^{21} N·m, equivalent to a moment magnitude M_W 8.3. If we consider only GPS measurements, we obtain the rupture model presented in Fig. 3b, which consists as well of a single slip patch but displaced to the north with a maximum slip of 4.8 m, seismic moment 2.51×10^{21} N·m, and moment magnitude M_W 8.2, consistent with the results of Tilmann et al. [36]. Finally, the coseismic model obtained from joint InSAR+GPS data inversion (Fig. 3c) yields a similar slip distribution as the model estimated using solely InSAR data, although with a more elongated slip patch and slightly higher maximum slip of 7.8 m, leading to a seismic moment of 3.64×10^{21} N·m and moment magnitude M_W 8.3. Considering only the main slip patch between the 30º and 32º latitude range approximately, the mean slip is 4.3 meters, which is rather consistent with the 4.9 m of elastic deformation accumulated since the 1943 rupture assuming a convergence rate of 68 mm/yr and full locking [6]. It is apparent from Fig.3b that a model based solely on GPS measurements leads to more restricted slip directions and magnitudes compared to those from combined GPS and InSAR data.

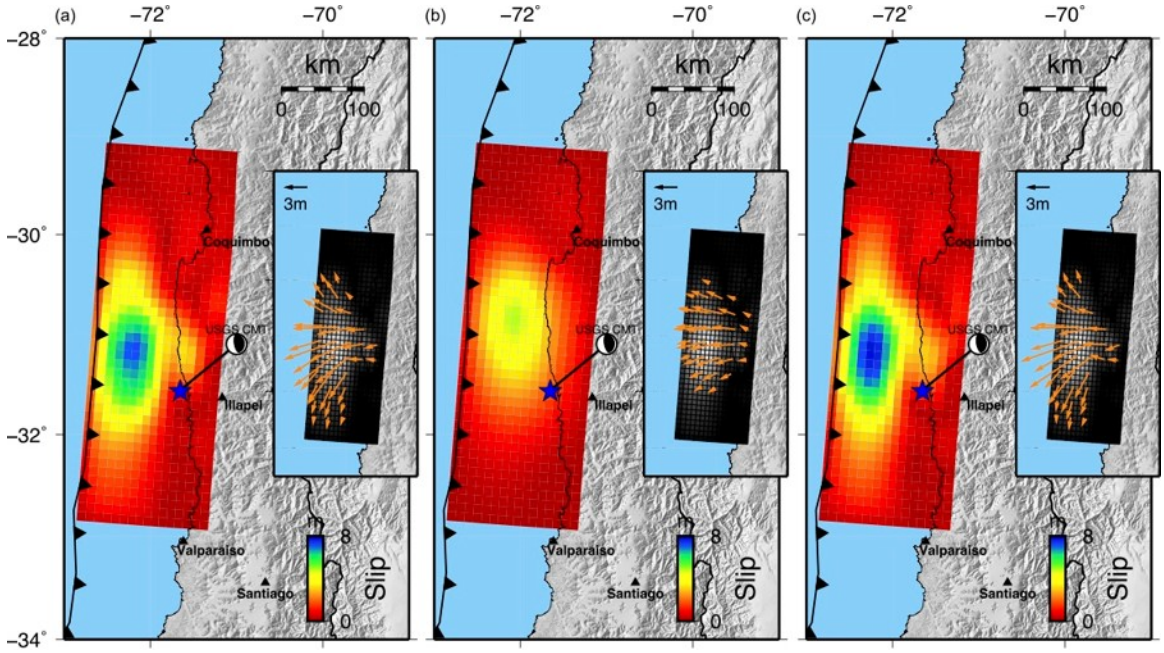

Fig. 3 – Distribution of slip magnitudes and directions for the Illapel earthquake as obtained from (a) InSAR inversion; (b) GPS; and (c) InSAR+GPS data. The small rectangle at the right of each panel shows the direction of the estimated slip on the rupture surface.

To test the solution for consistency, we predict surface displacements at different locations starting from

each of the obtained slip models as shown in Fig. 4. Blue and red arrows show horizontal and vertical displacement, respectively. Numbers above blue arrows indicate the magnitude in meters of the corresponding horizontal displacements at the coast. The directions of these displacements are in good agreement with the measured GPS data. As expected, all three models lead to higher surface displacements between 30º and 32º S, closer to the zone of maximum slip. For further verification, we also generate synthetic ascending and descending interferograms and compare them to the observed LOS deformation. This analysis yields root mean squared errors of 0.0114 (0.0153) meters for the ascending (descending) interferogram if we only use InSAR data, and 0.0104 (0.0127) meters for the ascending (descending) orbit if GPS observations are included. In summary, joint use of InSAR and GPS data leads to an error decrease of the order of 8% to 17% in the predicted coseismic deformation field, as compared to models based exclusively on InSAR inversion. Hence, we base the subsequent analysis and conclusions on the combined slip model.

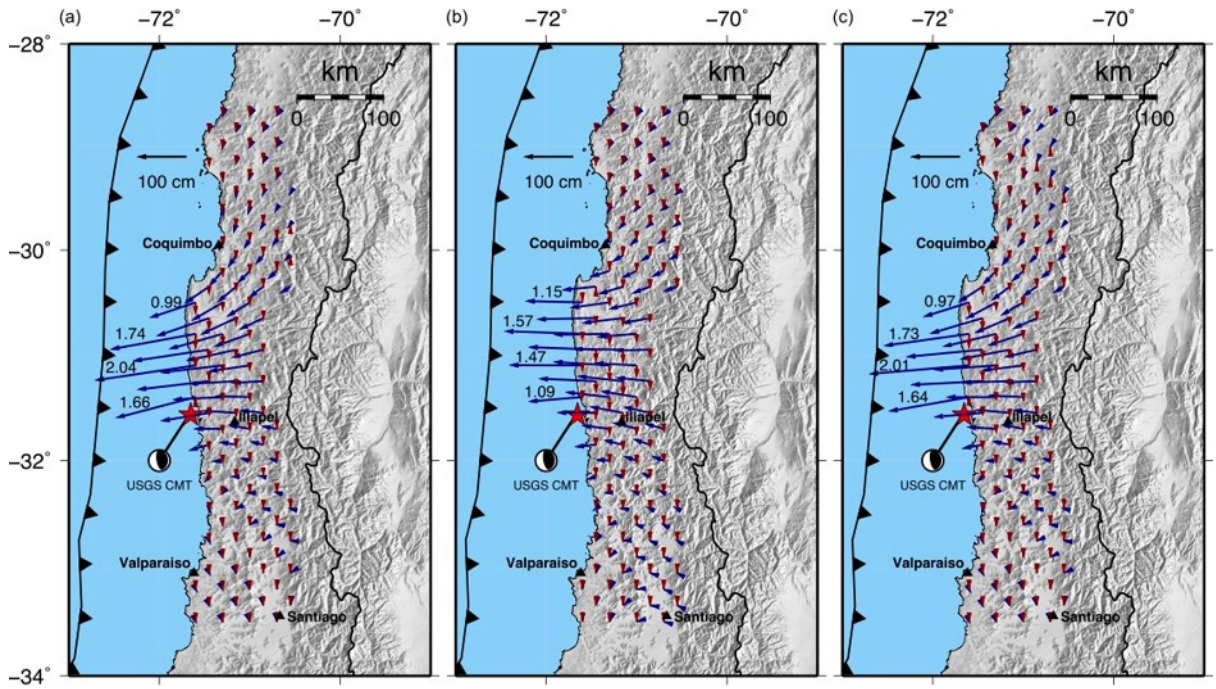

Fig 4. – Predicted surface displacements corresponding to slip models based on (a) InSAR; (b) GPS; and (c) InSAR+GPS data. Blue and red arrows indicate horizontal and vertical displacements, respectively, with a length scale indicated by the top black arrow.

We used the InSAR+GPS slip distribution and fault geometry to calculate the Coulomb failure stress change induced by the M_W Illapel earthquake, adopting however an average constant dip angle due to software constraints. Our results are shown as a projected color map in the top panel of Fig.5, together with the location of all M_w≥5.0 aftershocks, location and color-coded magnitude of M_w≥6.0 aftershocks, plus date and focal mechanisms for the main shock and subsequent events with available CMT solutions [3]. In the bottom panel, we show the location and magnitude of M_w≥6.0 aftershocks relative to the Slab 1.0 profile (red dashed line), following the same color scheme as in the top panel.

This figure evidences a strong correlation between regions where Coulomb stress is increased (red areas) as consequence of the earthquake, and the occurrence of the most relevant aftershocks. The main slip patch seen in Fig. 3 correlates as expected with a significant stress release (blue patch), but induces as well a region of increased loading immediately to the East, that coincides with the location of several strong aftershocks, including a M_w 7.6 event shortly after the main shock. A similar trend is seen to the North at latitudes around 30.5º S and to the South at latitudes ~32ºS, locus of continued M_w>5.0-6.0 seismic activity in the following month. However, the swarm of shocks registered on November 2015 at latitudes ~29ºS falls over a region of

zero CFS increase, so it cannot be immediately attributed to induced tectonic loading.

Inspection of the depths and focal mechanisms of M_w≥6.0 aftershocks shows that the Illapel earthquake sequence largely follows the subduction geometry and take place at depths close to those of the Slab 1.0 model [27], and those with available CMT solutions are found to be originated by a thrust mechanism similar to the initial event. The only identified outlier in this trend is the M_W 6.7 aftershock on September 21st, for which the moment tensor centroid is located ~ 25 km above the slab's expected depth. In general, the locations of this seismic sequence are consistent with the coupling analysis in Métois et al. [6], which shows that, at latitude 30°S, the plate coupling coefficient reaches values ~60% down to depths of about 50 km, and decreases significantly down dip, indicating a concentration of elastic strain energy in the shallower parts of the subduction interface.

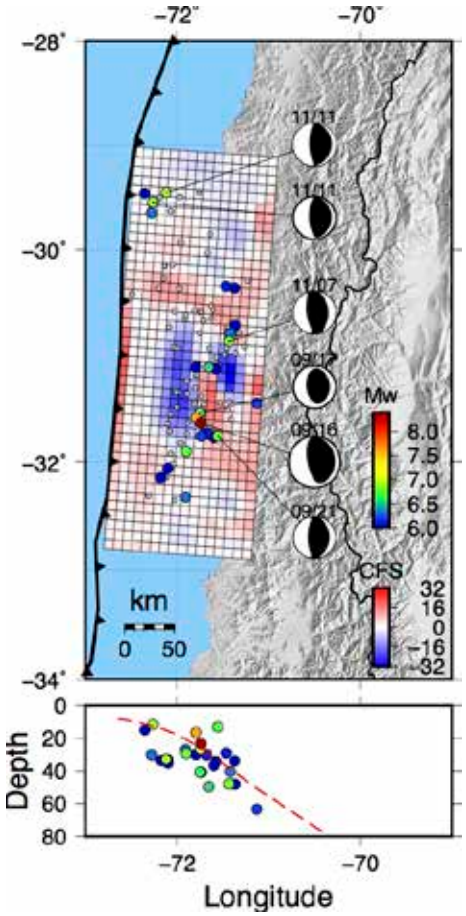

Fig 5. – Coulomb stress change and aftershocks for the Illapel earthquake. In the top panel, the projected color map shows the changes in Coulomb failure stress (CFS) over the fault plane after the M_w 8.4 earthquake. Stress values are represented according to the bottom color scale, in units of bar. We also plot the location of all M_w≥5.0 aftershocks (up to two months after the earthquake) as gray dots, and highlight M_w≥6.0 events represented by larger color-coded circles whose corresponding magnitudes can be read from the top color scale. Beach-balls represent the focal mechanisms for all events with available CMT solutions, identified by their date of occurrence. In the bottom panel, we plot the projected depth of M_w≥6.0 aftershocks, and the Slab 1.0 profile (red dashed line).

5. Slip Distribution Models for Recent Chilean Earthquakes.

Our team has performed a similar InSAR and inversion analysis as described here for the other two most significant earthquakes occurred in Chile in the last decade, the M_W 8.8 Maule earthquake on February 27th 2010 (27F), and the M_W 8.2 Pisagua earthquake on April 1st 2014 (1A). The slip distributions obtained are shown in

Fig. 6, and our fault model for 27F was published and described in detail elsewhere [28]. In general, the three events can be described as megathrust earthquakes that released elastic strain energy accumulated over several decades of subsidence of the Nazca Plata under the South American plate in areas of high tectonic coupling. For the 2010, the rupture was bilateral and shows two patches of significant slip with maximums of 13.4 and 10.2 m, which is in agreement with other studies [37-39], and consistent with a practically full release of the interseismic stress build up since the M_W 8.5 Concepción earthquake in 1835 [40]. In section 4, it was argued that the Illapel slip distribution also implies a full relaxation of stress accumulated since the previous full rupture in 1943, but the post-earthquake scenario for northern Chile region affected by 1A is different. In this case, our inversion model yields a maximum slip of only 4 m, which accounts for only a fraction of the estimated 8.6 m deficit accrued since the M_w 8.8 1877 earthquake, assuming full locking and a convergence rate of 63 mm/yr [41]. Recent research suggests indeed that the M_W 8.2 earthquake is not the major earthquake expected in this region and that there is continuing megathrust potential in the north of Chile [42]. Hence, understanding both the faulting mechanisms behind past and possible future earthquakes and of their effects in terms of ground motions, is instrumental to an improved hazard awareness and preparation.

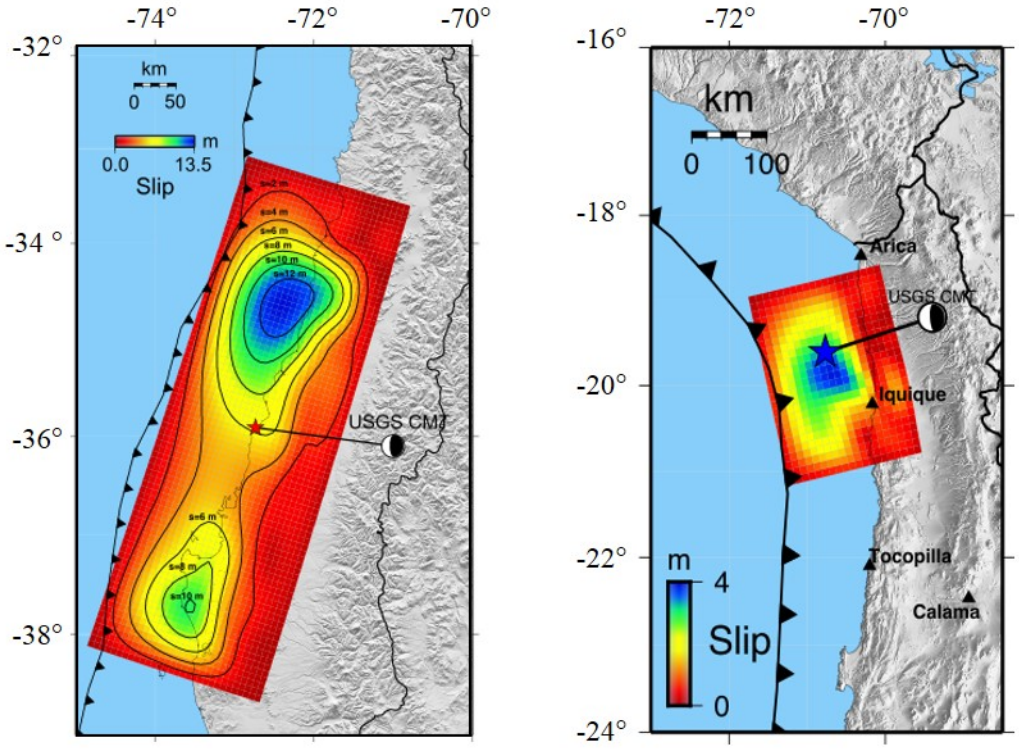

Fig. 6 – Slip models for the February 27th 2010 Maule earthquake (left), and the April 1st 2014 Pisagua earthquake (right).

All studies combined, we have generated methodologically consistent and spatially detailed characterizations of the fault rupture mechanisms and the permanent superficial effects of three recent megathrust events distributed along the Chilean coastline. Beyond the geophysical knowledge that is gained from such a research exercise, these results are also highly valuable from the perspective of earthquake structural design and risk analysis. Concretely, they can be used to reconstruct the low- and high-frequency components of the ground motions caused by the earthquake at different points on the surface, and thereby provide a physically plausible representation of the seismic demand experienced by buildings across the affected region. In previous work, we have proposed a methodology based on the use of Green's functions to compute synthetic low-frequency seismic records that are consistent with the InSAR coseismic displacement field [28], and that can be combined with stochastic or deterministic physics-based models that account for the high-frequency component of ground motions, like the Specific Barrier Model (SBM; [43,44]). Our current work is focused on the calibration of the latter to subduction zone earthquakes using a ground motion record database that comprises

309 Chilean seismic events since 1985 and a worldwide database of similar ground motions. This process requires as well knowledge on the slip distribution for the most relevant events, and hence relies on the results contained in Figs. 3 and 6. The scheme thus developed will be suitable for region-dependent predictions of strong motion parameters (e.g. peak ground acceleration, spectral response) and the simulation of broadband time histories, which is an urgent need in a country like Chile that is widely recognized for its intense seismic activity, yet lacks a dense array of strong ground motion instruments that could serve as a basis for the development of specific ground motion prediction equations.

6. Conclusions.

We have used satellite SAR observations obtained closely before and after the 2015 M_W Illapel earthquake to determine the field of coseismic displacements in the region of north Chile extending from latitude ~29ºS to 33ºS. Observations from both ascending and descending orbits of Sentinel 1A reveal a maximum line-of-sight surface deformation of 1.4 m registered north of the earthquake's epicenter at latitude ~31ºS. Detailed inspection of interferogram local features suggest occurrence of site effects that may be associated with tailing dams deformations in Chile's region IV. These data are combined with continuous GPS measurements in a joint seismic inversion to infer the geometry and distribution of slip in the subduction interface. The best-fit model corresponds to a 420 × 160 km rupture surface defined by a constant strike of 4º and variable dip angle ranging from 2.7º to 24.3º, with a single principal slip patch with maximum slip of 7.8 m, total seismic moment of 3.64×10^{21} N·m and moment magnitude M_W 8.3. Comparison of predicted and observed surface displacements shows that joint InSAR+GPS inversion leads to smaller errors in the range between 8% and 17% relative to models that rely solely on InSAR data. Based on our slip distribution, we studied the transfer of Coulomb stress across the rupture surface after the main shock, and found a good correspondence between areas of increased stress and the location of subsequent aftershocks.

In addition to the Illapel earthquake, we have conducted similar InSAR-based analysis of faulting mechanisms for the Maule 2010 and Pisagua 2014 earthquakes, thus generating a robust and consistent set of slip models for subduction earthquakes along the Chilean territory. These results provide a wealth of information regarding the geophysics of past and likely future subduction events, allowing a better assessment of seismic hazards and identification of areas of increased risk. From the engineering perspective, our work is now focused in using these models as an input for the generation of synthetic seismic records that provide a reliable representation of low- and high-frequency components of ground motions, which must be respectively consistent with coseismic surface deformations, and with the distribution of slip within the plate interface. In this way, we will able to characterize the seismic demand for both flexible and rigid structures in earthquake-affected areas, and thus improve estimates of —and prepare for— the direct damage and losses that may be expected during future events.

7. Acknowledgements

This work has been sponsored by the National Research Center for Integrated Natural Disaster Management (CIGIDEN), CONICYT/FONDAP 15110017, and by the National Commission for Scientific and Technological Research (CONICYT) under grant Fondecyt 1141187. The authors also acknowledge support from University of Notre Dame College of Engineering – PUC School of Engineering Seed Fund Project 14ENI2-26862.

8. References

[1] U.S. Geological Survey, USGS (2015), http://earthquake.usgs.gov/earthquakes/ eventpage/us20003k7a
[2] Oficina Nacional de Emergencias del Ministerio del Interior y Seguridad Pública, ONEMI (2015), http:\\www.onemi.cl.
[3] Global Centroid Moment Tensor Project, CMT (2015), http://www.globalcmt.org/.
[4] Ekström, G., Nettles, M. & Dziewonski, A.M., (2012): The global CMT project 2004-2010: Centroid-moment tensors for 13,017 earthquakes, *Phys. Earth Planet. Inter.*, 200,1.
[5] Centro Sismológico Nacional, CSN (2015), www.sismologia.cl.
[6] Métois, M., A. Socquet, and C. Vigny (2012): Interseismic coupling, segmentation and mechanical behavior

of the central Chile subduction zone. *Journal of Geophysical Research (Solid Earth)*, 117, B03406.
[7] Lomnitz, C. (2004): Major earthquakes of Chile: A historical survey, 1535-1960. *Seismol. Res. Lett*., 75, 368–378.
[8] Nishenko, S. P. (1991): Circum-Pacific seismic potential: 1989 1999. *Pure and Applied Geophysics*, 135, 169–259.
[9] Comte, D., A. Eisenberg, E. Lorca, M. Pardo, L. Ponce, R. Saragoni, S. K. Singh, and G. Suarez (1986): The 1985 Central Chile Earthquake: A Repeat of Previous Great Earthquakes in the Region?. *Science*, 233, 449–453.
[10] Lomnitz, C. (1971): Major earthquakes and Tsunamis in Chile during the Period 1535 to 1953. *Geol Rudnsch*, 59, 938–960.
[11] Beck, S., S. Barrientos, E. Kausel, and M. Reyes (1998): Source characteristics of historic earthquakes along the central Chile subduction zone. *Journal of South American Earth Sciences*, 11, 115–129.
[12] Malgrange, M., A. Deschamps, and R. Madariaga (1981): Thrust and extensional faulting under the Chilean coast: 1965, 1971 Aconcagua earthquakes. *Geophysical Journal*, 66, 313–331.
[13] Pardo, M., Compte, D., Monfret, T. et al. (2002): The October 15, 1997 Punitaqui earthquake (Mw=7.1): a destructive event within the subducting Nazca plate in central Chile. *Tectonophysics*, 345, 199.
[14] Tichelaar, B. W., and L. J. Ruff (1991): Seismic coupling along the Chilean Subduction Zone. *J. Geophys. Res.,* 96, 11,997.
[15] Yáñez, G. A., C. R. Ranero, R. von Huene, and J. Díaz (2001): Magnetic anomaly interpretation across the southern central Andes (32º-34ºS): The role of the Juan Fernández Ridge in the late Tertiary evolution of the margin. *J. Geophys. Res.*, 106, 6325–6345.
[16] Arriagada, C., P. Roperch, C. Mpodozis, R. Charrier, G. Yanez, and M. Farias (2009): The Vallenar Discontinuity and the Maipo Orocline: Regional significance of clockwise vertical-axis rotations in the central Chilean Andes. *AGU Spring Meeting Abstracts*, p. A4.
[17] Heinze, B. (2003): Active intraplate faulting in the forearc of north central chile (30º-31ºS). Implications from neotectonic field studies, gps data, and elastic dislocation modeling, *Ph.D. Thesis, Free University, Berlin.*
[18] González, G., J. Cembrano, D. Carrizo, A. Macci, and H. Schneider (2003): The link between forearc tectonics and Pliocene-Quaternary deformation of the Coastal Cordillera, northern Chile. *Journal of South American Earth Sciences*, 16, 321–342.
[19] Allmendinger, R. W., and G. González (2010), Invited review paper: Neogene to Quaternary tectonics of the coastal Cordillera, northern Chile, Tectonophysics, 495, 93–110, doi:10.1016/j.tecto.2009.04.019.
[20] Cortés, J., González, G., Binnie, S. et al. (2012): Upper-plate fault activity in northern Chile: An integrated paleoseismological and numerical modeling approach*, Congreso Geologico Chileno.*
[21] Massonnet, D., & Feigl, K.L., (1998): Radar interferometry and its application to changes in the earth's surface, *Reviews of Geophysics*, 36, 4441.
[22] Rosen, P., Hensley, S., Joughin, I. et al., (2000): Synthetic aperture radar interferometry, *Proceedings of the IEEE*, 88,333.
[23] Hanssen, R.F., (2001): Radar interferometry: data interpretation and error analysis, *Kluwer Academic Publishers*, 308 pp.
[24] Werner, C., U. Wegmüller, T. Strozzi, and A. Wiesmann (2000): Gamma SAR and interferometric processing software, in *ERS-ENVISAT Symposium*, Gothenburg, Sweden.
[25] Okada, Y. (1985): Surface deformation due to shear and tensile faults in a half-space. *The Bulletin of the Seismological Society of America*, 75, 1135–1154.
[26] Jonsson, S. (2002): Fault Slip Distribution of the 1999 Mw 7.1 Hector Mine, California, Earthquake, Estimated from Satellite Radar and GPS Measurements. *The Bulletin of the Seismological Society of America*, 92, 1377–1389.
[27] Abell, J., J. C. de la Llera, and C. W. Wicks (2011): Enhancement of long period com-ponents of recorded and synthetic ground motions using InSAR, *Soil Dynamics and Earthquake Engineering*, 31, 817–829.
[28] Fortuño, C., J. C. de la Llera, C. W. Wicks, and J. A. Abell (2014): Synthetic Hybrid Broadband Seismograms Based on InSAR Coseismic Displacements. *The Bulletin of the Seismological Society of America*, 104, 2735–2754.
[29] Okada, Y. (1992): Internal deformations due to shear and tensile faults in a half-space. *The Bulletin of the Seismological Society of America*, 82, 2, 1018.

[30] King, G., Stein, R. & Lin, J. (1994): Static Stress Changes and the Triggering of Earthquakes. *The Bulletin of the Seismological Society of America*, 84, 3, 935.
[31] Lin, J. & Stein, R. (2004): Stress triggering in thrust and subduction earthquakes and stress interaction between the southern San Andreas and nearby thrust and strike-slip faults. *Journal of Geophysical Research*, 109, B02303.
[32] Toda, S., R. S. Stein, K. Richards-Dinger & S. Bozkurt, (2005): Forecasting the evolution of seismicity in southern California: Animations built on earthquake stress transfer, *Journal of Geophysical Research*, 110, B05S16.
[33] Hayes, G. (2015): Preliminary finite fault results for the sep 16, 2015 Mw 8.3 46 km W of Illapel, Chile earthquake (version 1), *http://earthquake.usgs.gov/earthquakes/eventpage/ us20003k7a#scientific_finitefault.*
[34] Hayes, G. P., D. J. Wald, and R. L. Johnson (2012): Slab1.0: A three-dimensional model of global subduction zone geometries. *Journal of Geophysical Research (Solid Earth),* 117, B01302.
[35] Béjar-Pizarro, M., A. Socquet, R. Armijo, D. Carrizo, J. Genrich, and M. Simons (2013): Andean structural control on interseismic coupling in the North Chile subduction zone. *Nature Geoscience*, 6, 462–467.
[36] Tilmann, F., Y. Zhang, M. Moreno, J. Saul, F. Eckelmann, M. Palo, Z. Deng, A. Babeyko, K. Chen, J. C. Baez, B. Schurr, R. Wang, and T. Dahm (2016): The 2015 Illapel earthquake, central Chile, a type case for a characteristic earthquake?. *Geophysical Research Letters*, 43,2.
[37] Pollitz, F. F., Brooks, B., Tong, X., et al. (2011). Coseismic slip distribution of the February 27, 2010 Mw 8.8 Maule, Chile earthquake, *Geophysical Research Letters* 38, 9.
[38] Vigny, C., A. Socquet, S. Peyrat, et al. (2011): The 2010 Mw 8.8 Maule Megathrust Earthquake of Central Chile, Monitored by GPS, *Science,* 332, 1417.
[39] Tong, X., D. Sandwell, D., Luttrell, K., et al. (2010): The 2010 Maule, Chile earthquake: Downdip rupture limit revealed by space geodesy, *Geophysical Research Letters* 37, 24.
[40] Moreno, M., Melnick, D., Rosenau, M. et al. (2011): Heterogeneous plate locking in the South–Central Chile subduction zone: Building up the next great earthquake, *Earth and Planetary Science Letters*, 305, 413.
[41] Chlieh, M., Perfettini, H., Tavera, H. et al. (2011): Interseismic coupling and seismic potential along the Central Andes subduction zone, *Journal of Geophysical Research*, 16, B12405.
[42] Hayes, G., Herman, M., Barnhart, W. et al. (2014): Continuing megathrust earthquake potential in Chile after the 2014 Iquique earthquake, *Nature*, S12
[43] Papageorgiou, A. S., & K. Aki (1983a). A specific barrier model for the quantitative description of inhomogeneous faulting and the prediction of strong ground motion. I. Description of the model, *Bull. Seism. Soc. Am.* 73, 693-722.
[44] Papageorgiou, A. S., & K. Aki (1983b). A specific barrier model for the quantitative description of inhomogeneous faulting and the prediction of strong ground motion. II. Applications of the model, *Bull. Seism. Soc. Am.* 73, 953-978.